Continental Shelf Research 147 (2017) 102–113

Contents lists available at ScienceDirect

Continental Shelf Research

journal homepage: www.elsevier.com/locate/csr

Spatially varying drag within a wave-exposed mangrove forest and on the adjacent tidal flat

Julia C. Mullarney[a,*], Stephen M. Henderson[b], Johan A.H. Reyns[c,d], Benjamin K. Norris[a], Karin R. Bryan[a]

[a] Coastal Marine Group, Faculty of Science and Engineering, University of Waikato, Hamilton, New Zealand
[b] Washington State University, Vancouver, Washington, USA
[c] IHE Delft, Delft, The Netherlands
[d] Deltares, Delft, The Netherlands

ARTICLE INFO

Keywords:
Mekong Delta
Mangroves
Flow rotation
Drag coefficients
Vietnam
Friction

ABSTRACT

Mangroves have been shown to protect shorelines against damage from the combined hydrodynamic forces of waves and tides, owing to the presence of roots (pneumatophores) and tree trunks that enhance vegetative drag. However, field measurements within these environments are limited. We present field observations of flows from the seaward coast of Cù Lao Dung Island (Sóc Trăng Province) in the Mekong Delta, Vietnam. Measurements were made in two different seasons along a transect that crosses from mudflats to mangrove forest. Flows are also explored using an idealised numerical model. Both the data and model capture the flow transitions from mudflat across the fringing region to the forest interior. We observe a rotation of the obliquely incident flows toward an orientation nearly perpendicular to the vegetated/unvegetated boundary. The momentum balances governing the large-scale flow are assessed and indicate the relative importance of friction, winds and depth-averaged pressure forces. In the forest, drag coefficients were 10–30 times greater than values usually observed for bottom friction, with particularly effective friction in the regions of dense pneumatophores at the fringe and when water depths were lower than the height of the pneumatophores. Pressure gradient balances suggest that the drag induced by bottom friction from pneumatophores was dominant relative to drag from the larger, but sparser, tree trunks.

1. Introduction

Mangrove forests across the globe support a myriad of physical and ecosystem services, and there has been increasing recognition of the economic value of this natural resource (Costanza et al., 1997; Barbier et al., 2008; Perillo et al., 2009). These highly productive ecosystems provide vital habitat for diverse fauna (fish, birds, reptiles and shellfish) (Kathiresan and Bingham, 2001; Alongi, 2002). Moreover, tropical mangrove forests, in particular, also have high carbon-burial efficiency (Chmura et al., 2003; Donato et al., 2011; Mcleod et al., 2011). In addition to the ecological services provided, mangroves have been shown to buffer shorelines from damage by tidal currents (Mazda et al., 1997), waves (Massel et al., 1999; Mazda et al., 2006; Vo-Luong and Massel, 2008; Bao, 2011; Horstman et al., 2014) and tsunamis (Danielsen et al., 2005; Wolanski, 2007; Alongi, 2008). However, despite their ecological and physical utility, around half of total global mangrove coverage has been lost since pre-industrial times (Giri et al., 2011). The most dramatic changes have occurred in developing and densely populated areas such as the Mekong Delta in Vietnam, largely owing to resource requirements and land-use changes in the last few decades, (e.g. the conversion of mangrove regions to shrimp aquaculture ponds; Thu and Populus, 2007; Nguyen et al., 2013). Indeed, recent studies of the Sông Hậu distributary in the Mekong Delta have reported a lower sediment supply to the coast (Nowacki et al., 2015) than previous estimates, likely due to construction of dams upstream (Wolanski et al., 1996) and secondarily to a significant increase in channel-bed sand mining over the last decade (Anthony et al., 2015).

Furthermore, the vulnerability of these regions is also increasing in the face of climate change and sea-level rise (Nicholls et al., 1999; Sallenger et al., 2012; Knutson et al., 2010). Understanding the ability of mangroves to exert hydrodynamic drag, and consequently to trap and retain sediment to mitigate against erosion, is therefore a key step in the prediction of the geomorphic evolution of these regions. In particular, a key question is whether mangroves can promote sufficient

* Corresponding author.
E-mail addresses: julia.mullarney@waikato.ac.nz (J.C. Mullarney), steve_henderson@vancouver.wsu.edu (S.M. Henderson), j.reyns@unesco-ihe.org (J.A.H. Reyns), bkn5@students.waikato.ac.nz (B.K. Norris), kbryan@waikato.ac.nz (K.R. Bryan).

http://dx.doi.org/10.1016/j.csr.2017.06.019
Received 12 October 2016; Received in revised form 3 June 2017; Accepted 24 June 2017
Available online 27 June 2017
0278-4343/

accretion (acting as 'ecosystem engineers') to allow the forest to keep pace with sea-level rise, as hypothesized may occur with salt marshes (Kirwan et al., 2010, 2016; Mariotti and Fagherazzi, 2010).

Aquatic vegetation (including mangroves) enhances drag and dissipates hydrodynamic energy (Nepf, 1999). This reduction of energy induces slow flow zones which encourage sediment deposition (e.g. Krauss et al., 2003; Walsh and Nittrouer, 2004). The extent to which drag is enhanced depends strongly on the form of the mangroves (Mazda et al., 1997) and the width of the vegetation cover. Mullarney and Henderson (2017) suggest that a forest or marsh width of $L = (2gD\eta/a)^{1/3}$ is required to dissipate longer period flows (assuming a flat bed, and where a is the frontal-area density of the vegetation, g is acceleration due to gravity, and η and D are the surge/tide height and duration, respectively). However, even for smaller widths L, vegetation has ability to alter flow directions, attenuate shorter-period waves and modify turbulence characteristics (Norris et al., 2017). In particular, vegetative drag dominates over bottom friction for most forms of aquatic vegetation (when $al > 4 \times 10^{-3}$, where l is vegetation height, see Mullarney and Henderson, 2017 for scaling analysis). Although field observations from mangrove forests are still relatively rare in comparison to similar measurements from salt marshes, previous measurements have reported large friction coefficients in dense mangrove forests (Furukawa et al., 1997, observed Manning friction coefficients within the forest as four times greater than those measured in adjacent tidal creeks). This vegetation-induced friction can result in complex flow paths with jets, eddies and stagnation zones. Flow paths within mangroves can depend strongly on bathymetry, which is often complex and channelised. Recent work from a tropical mangrove forest with incised creeks reported rotation of the flow, from creek-parallel in the channel to creek-perpendicular within the mangroves at higher water levels (Horstman et al., 2013).

Despite substantial vegetation heterogeneity, models for flows within mangrove forests often assume uniform (macro) roughness and dispersion coefficients (Wolanski et al., 1980; Struve et al., 2003; Mazda et al., 2005; van Maanen et al., 2015). Here, we report measurements of flow dynamics from a mangrove forest in the Mekong Delta, Vietnam. The primary objective was to quantify how drag varies over the differing environments in the system (mudflat, fringe and forest interior) and to explore how any changes in drag affect current speeds and directions. The focus here is on wave-averaged currents (for examination of wave dynamics, see Henderson et al., 2017). Unlike many forests considered by previous studies, the forest here is exposed directly to waves from the Vietnamese East Sea (also known as the South China Sea). Moreover, strong winds were common over the tidal flats adjacent to the forest. The forest fringe is characterised by a relatively straight edge, with no creeks in the vicinity of the instrument deployment sites. Section 2 describes the field site and instrument deployments. Section 3 presents the data in which we observe a dramatic large-scale flow rotation abruptly as the flow enters the forest on flood tide. In Section 4, we consider momentum balances to obtain estimates for drag coefficients and discuss the implications of the underlying dynamics. These balances are further explored with use of an idealised numerical model in Section 5, and values are compared with previous work. Finally, conclusions are presented in Section 6.

2. Field measurements

2.1. Field site

Field observations were undertaken in a mangrove forest which lines the seaward shore of Cù Lao Dung Island of the Mekong Delta, Vietnam (Fig. 1a) (Wright, 1985). The fringe region of the forest is predominantly composed of *Sonneratia caseolaris* trees. Tree density is greatest at the fringe with cover becoming sparser farther into the forest (Bullock et al., 2017). The wide southwest side of the forest is prograding rapidly, with a relatively sandy substrate and a gentle topographic slope of approximately 1 in 800 (Fig. 1b). Conversely, on the northeastern side, the forest is narrower, older and the muddy substrate is eroding. The NE side is also steeper with a topographic slope of about 1 in 200 (Bryan et al., 2017). In front of the island, a shallow tidal flat of interlaminated mud-and-sand deposits extends for several kilometres (Fricke et al., 2017). Wave energy from the South China Sea can propagate directly over this flat into the fringe. Field experiments were undertaken in September to October in 2014 and March 2015. Conditions were relatively quiescent in September and October 2014, with lower wind speeds and small wave heights, whereas conditions during March 2015 were marked by stronger winds and larger waves (significant wave heights near the forest fringe reached a maximum of 0.72 m).

2.2. Measurements

Measurements were focused around two transect lines covering the mudflat-to-fringe transition, with instruments deployed up to 150 m either side of the fringe ($x = 0$). Velocimeters (ADVs), Acoustic Doppler Current Profilers (ADCPs), and pressure sensors were moved around over a number of short-term deployments 1–2 days) with total experiment durations of 6 and 7 days on the SW side in 2014 and 2015, respectively, and 2 days on the NE side in both 2014 and 2015. Velocimeters (Nortek Vectors) and pressure sensors (RBR Solo-P) sampled continuously at 32 and 0.5 Hz, respectively. ADCPs (2 MHz Nortek Aquadopps) operated in pulse-to-pulse coherent mode to obtain high-frequency measurements at 8 Hz almost continuously (burst lengths of 512 s with a 3-s separation between bursts). Aquadopps sampled at 25-mm vertical resolution over short profile lengths of 0.45 m (SW side) and 0.22 m (NE side). Throughout the 2015 field campaign, a weather station (Hobo U30) was placed ~130 m in front of the fringe at the SW side of the island, 3.6 m above the tidal flats, and recorded atmospheric pressure, wind speed and direction every minute. Wind speeds inside the forest ($x = 30$ m at a height of ~3.5 m above the bed) were also measured for a period of ~6 days. In 2014, only atmospheric pressure was recorded, so 6-hourly wind velocities (at 10 m) were obtained from the NCEP/DOE AMIP-II Reanalysis Model (https://www.esrl.noaa.gov/psd/data/gridded/data.ncep.reanalysis2.html). Deployment settings are summarised in Table 1.

Pneumatophore characteristics within a 1-m^2 quadrat placed in the vicinity of the acoustic instruments were obtained using both hand measurements and the photogrammetric method of Liénard et al. (2016). These vegetation statistics were used to calculate the frontal-area density a (m^{-1}) (the plant area in the plane perpendicular to the flow, per unit volume) as a function of height z (m). In total, 9 quadrats within the fringe and forest area were analysed.

2.3. Data analysis

ADCP velocities were processed to remove low-quality data (correlations <70%) and phase wraps (Lohrmann et al., 1990). ADV velocities were also processed to remove low-quality data (low correlations <70% or low signal-to-noise ratios) and spikes (Goring and Nikora, 2002). Data gaps were filled with a linear (small gaps $\lesssim$100 data points) or spectral fill (larger gaps) and cubic interpolation after despiking. All velocity data were rotated into across-shore (u), along-shore (v), and vertical (w) components. RBR (solo D) pressure sensors were leveled approximately to the same datum by assuming a flat water level at high tide (referenced to the instrument on the flats). These instruments were placed in thermally insulated flasks with small openings at the top to reduce temperature-dependent errors and were buried and covered by a few cm of sand, so that the resulting smooth seabed created minimal disturbance to pressure and flow fields. In 2015, the ADV on the flats was used to estimate significant wave heights every ten minutes, calculated as 4 times the standard deviation of the detrended sea-surface elevations after using linear wave theory to transform from measured values to surface values.

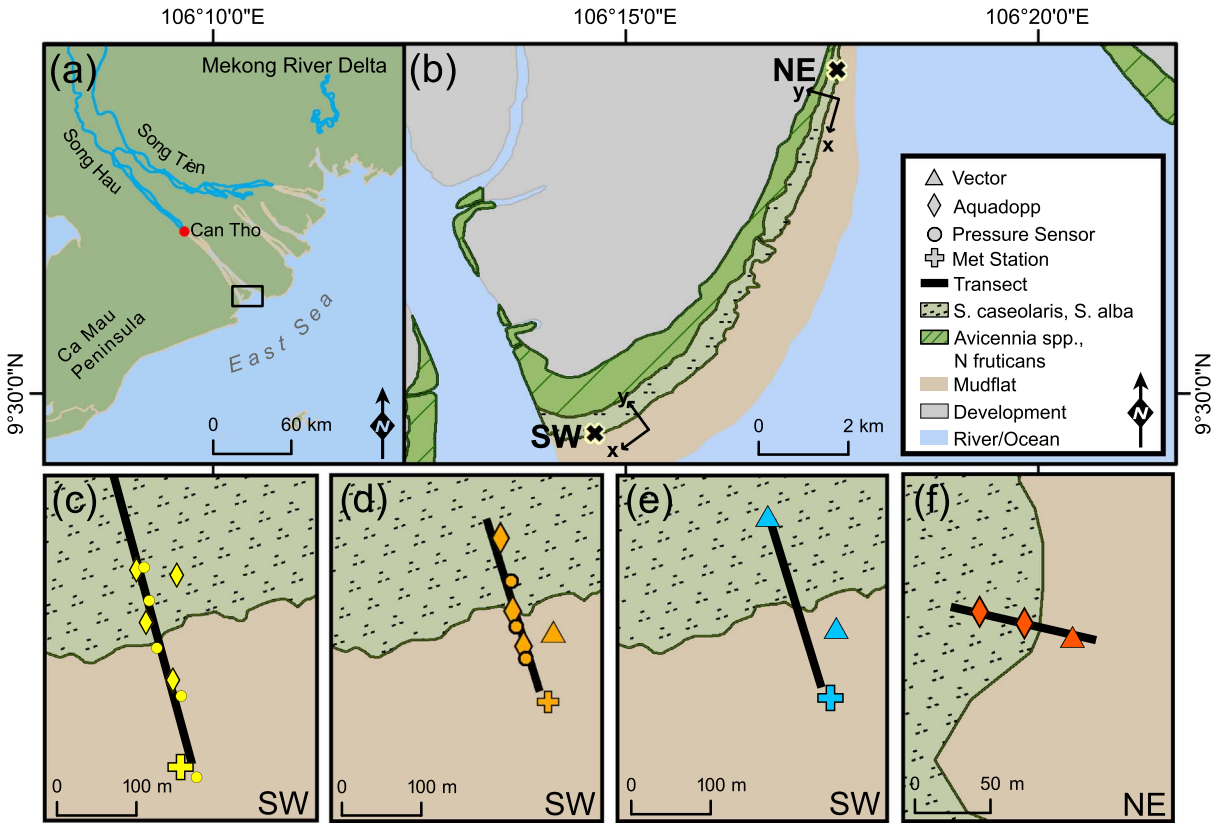

Fig. 1. (a) Mekong Delta showing location of Cù Lao Dung Island (black rectangle). (b) shows the main experimental sites (black x) on the relatively sandy SW and muddier NE sides of the island. (c) to (e) show instrument deployments on the SW side: (c) 'Flats to Forest' (F2F) experiment 2014, (d) 'Flats to Forest' (F2F) experiment 2015, (e) 'Fine Scale Study' (FSS) 2015. (f) shows the deployment on the NE side in 2015. Different symbols indicate different instrument types. The transition between mudflat (brown) and forest (light green) corresponds to the $x = 0$ location on across-shore transects.

3. Observations

3.1. Hydrodynamic and vegetation observations

In both seasons, high-tide water depths at the fringe were generally 1–1.5 m on the SW side, and 1.8 m on the NE side owing to the steeper bed gradient (Fig. 2 and see also Fricke et al., 2017). In March 2015, conditions on the mudflat were more energetic, with strong along-shore winds measured on most days (mean wind speeds up to 10 ms^{-1} and gusts to 13 ms^{-1}, Fig. 2). Winds decreased rapidly to nearly zero inside the forest (~1 ms^{-1} from wind sensor inside forest, not shown). Significant wave heights measured on the mudflat just in front of the forest reached 0.31 m in September and 0.72 m in March, with average periods of between 2 and 6 s. On some days wave breaking was observed offshore of the forest and at the forest fringe (for water depths $\gtrsim$ 0.5 m). Occasional wave breaking was observed at locations that were up to 100 m inside the forest.

Synoptic data from the differing environmental regions (mudflat, fringe and forest) in September showed (5-min averaged) velocities reaching up to 0.35 ms^{-1} on the mudflat and 0.15 ms^{-1} inside the forest during flood tide (within 0.5 m of the bed) (Fig. 3). As the tide propagated into the forest there was little reduction in the across-shore velocities but along-shore velocities were significantly reduced, indicating a substantial and abrupt rotation in the flow direction towards fringe-perpendicular (Fig. 4). Across-shore pressure gradients and velocities reversed at high tide. Flow rotation was observed in both breaking and non-breaking conditions. The most abrupt rotation occurred near the fringe, although additional rotation did occur farther into the forest (Fig. 4a, b). A similar rotation of flows to a fringe-perpendicular direction was seen at the NE deployment sites (Fig. 4c).

Vegetation surveys revealed significant spatial heterogeneity between the different deployment locations on the SW side. However, in general, pneumatophores were larger (both taller and with larger diameters) and denser within about 30 m of the fringe than in the forest interior (Norris et al., 2017). Pneumatophore statistics are shown in Table 2. The density of trees also decreased with distance inland (Bullock et al., 2017), but trees were taller in the interior (Nardin et al., 2016). On the NE side of the island, trees were older but

Table 1
Summary of the instruments deployed in September 2014 and March 2015 (Fig. 1). ADCPs (Nortek Aquadopps) were deployed with centre of profile ~0.3 m above the bed and ADV sampling volumes were ~0.4 m above the bed. Pressure sensors (P) were placed in vented, thermally insulating flasks, buried a few cm under the sediment surface. Across-shore positions are also given for these instruments, which were interspersed with pressure sensors along the transect. These instruments are listed in order, from outside of the fringe inwards. Negative sign indicates distance seaward from fringe.

Panel Fig. 1	Year	Experiment	Duration (M2 tides)	Instruments	Profiling range (m)	Sampling frequency (Hz)	Across-shore positions (x,m)
(c)	2014	F2F	2	ADCP×4, P×4	0.45	8, 0.5	−65, 5, 45, 75
(d)	2015	F2F	4	ADCP×3, P×4	0.45	8, 0.5	−50, 5, 95
(e)	2015	FSS	6	ADV×2,	–	32	−40, 125
(f)	2015	NE	2	ADV, ADCP×2	0.22	8, 32	−20, 10, 12
(d-f)	2015	All	all	Weather station, ADV	–	1/60, 32	−130, −40

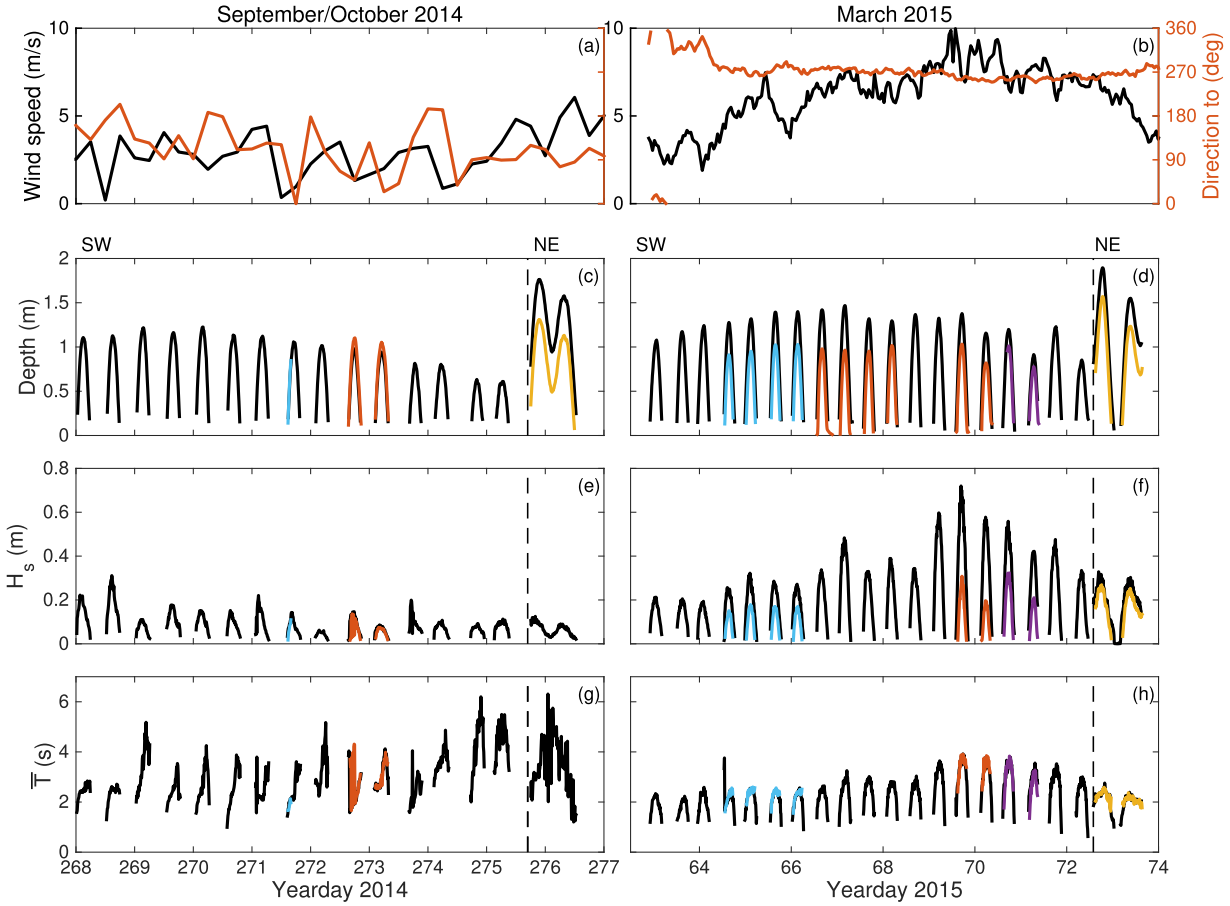

Fig. 2. Time series of conditions during the field experiments in 2014 (a,c,e,g) and 2015 (b,d,f,h). (a,b) Wind speed and directions, (c,d) Water depth, (e,f) significant wave height and (g,h) average wave periods. In panels c to g, the solid black line shows conditions from the mudflat just in front of the vegetation edge and coloured lines show data from different instruments inside the forest. In 2014 blue, orange, and yellow lines show instruments at x = 35, 75, and 50 m, respectively. In 2015, blue, orange, purple, and yellow, show data from instruments at x = 95, 120, 70 and 40 m, respectively. Times to the left and right of the dashed line indicate experiments on the SW and NE sides of the island, respectively.

more sparse in the fringe (Nardin et al., 2016). Although fewer quadrats were sampled, in general pneumatophores on this side appeared to be larger in diameter, consistent with the differences in tree age. Considering that the water depth at high tide was ~1.2 m and 1.6 m on the SW and NE sides, the water levels at the fringe were above the mean (maximum) height of the canopy for around 6 (3) hr and 9 (10) hr, respectively (noting that we measured on the NE side during neap tide only).

4. Estimates of drag coefficients

The rotation of flow as water entered the forest was observed on all days of the experiments under multiple forcing conditions. Here, we consider the along- and across-shore pressure balances to estimate the drag coefficients in the forest and fringe regions.

4.1. Across-shore drag balance

In order to examine drag coefficients, for simplicity we first neglect forcing by winds and waves (these additional forcing terms will be discussed below), assume steady conditions and neglect inertia. A depth-averaged across-shore balance between pressure and friction yields:

$$g\frac{d\eta}{dx} = -C_d|\mathbf{u}|u/h. \quad (1)$$

During the 'Flats to Forest' experiment in 2014, winds were light (<4.2 ms^{-1}), and measured waves were small (H_s < 0.18 m at the Aquadopp on mudflat) over the two tidal cycles. The left-hand side of Eq. (1) was calculated by differencing pressures measured at $x = -85, -20$, 32 and 71 m, while values for $|\mathbf{u}|u/h$ were calculated from Aquadopps at $x = -65$, 5 and 45 m (Fig. 1c). Velocity and pressure were averaged over 5-min intervals, and velocity was also averaged over the depth of the measured profile (the bottom ~0.5 m of water column). The resulting measurements of $gd\eta/dx$ and $|\mathbf{u}|u/h$ were then used in a linear fit to provide a single estimate of the bulk drag coefficient C_D for the flooding tide in different regions of the forest (Fig. 5a, C_D = negative slope of best-fit line). The significance of differences between fit coefficients were determined at the 95% confidence level using unpaired t-tests (here and in following sections). Outside of the forest (blue symbols), the pressure gradients were too small to be accurately resolved by the pressure sensors. However, larger pressure gradients across the fringe and forest regions yielded estimates of the drag coefficients as $C_D = 0.041$ in the fringe and $C_D = 0.032$ in the forest (with $r^2 = 0.75$ and 0.84, respectively). Hence, the drag was largest in the fringe, the region of most dense vegetation. Both values were an order of magnitude larger (18 and 14 times larger) than values typical of bottom friction in sand and mudflat environments (C_D=0.002). The strongest pressure gradients were observed when water depths were low (unfilled symbols, Fig. 5a). A fit for only these shallow cases yielded slightly but significantly larger, drag coefficients of $C_D = 0.047$ for the fringe, but not significantly larger coefficients $C_D = 0.033$ for the forest (with $r^2 = 0.95$ and 0.93, respectively). Therefore, friction appears to be greater when the water depths were less than, or comparable to, the height of the pneumatophores. Subtle differences between the incoming and outgoing tides were also

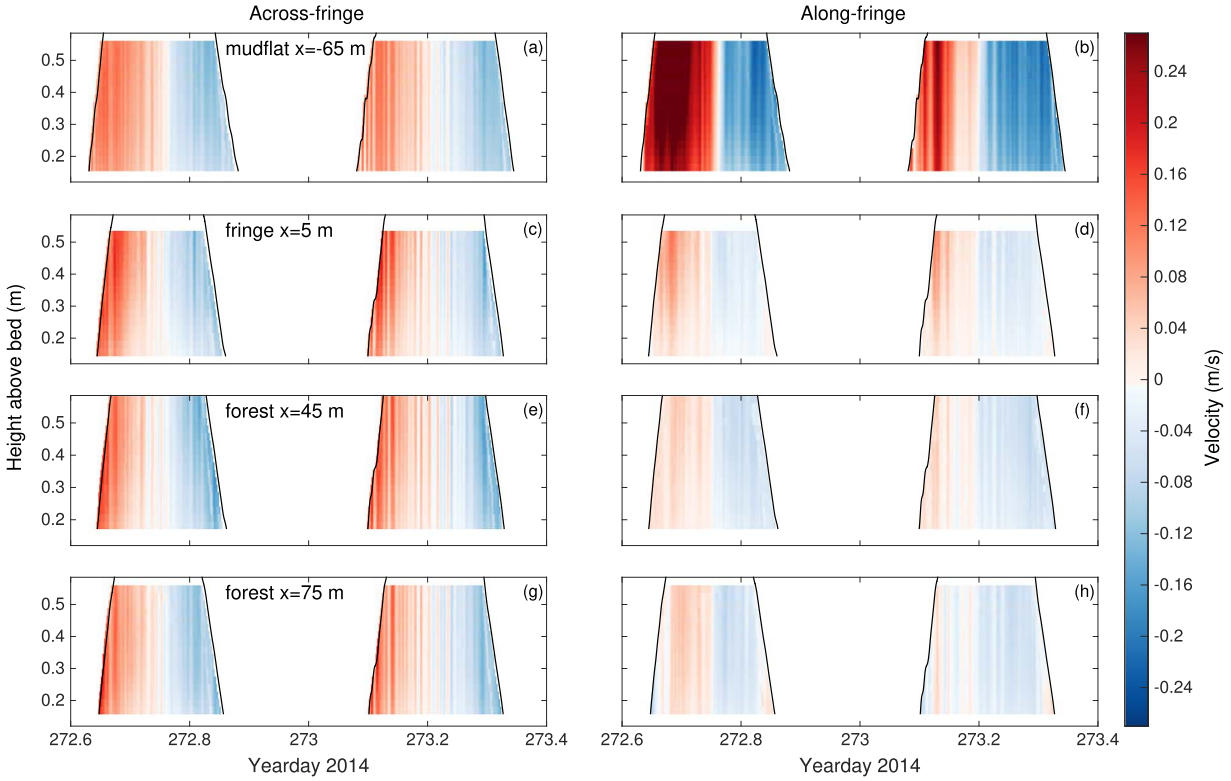

Fig. 3. Across-fringe (left-hand column) and along-fringe (right-hand column) velocities (5-min averages) and pressure (black line) from the SW of island for 'Flats to Forest' experiment in September 2014 (Fig. 1c). Velocities from instruments: on mudflat $x = -65$ m (a,b), at the fringe $x = 5$ m (c,d), and in the forest at $x = 45$ m (e,f) and $x = 75$ m (g,h).

apparent at the fringe (with points during ebb appearing to fall on a slightly steeper fit line).

If drag were predominantly supplied by the tree trunks that extend through the depth of the water column at all stages of the tide, and not the pneumatophores that change from emergent to submerged as the water depth increases, then the quality of the fit would be improved by instead plotting $g\mathrm{d}\eta/\mathrm{d}x$ against $|\mathbf{u}|u$ (hereafter, we call this the "emergent stem" model). However, in this case, the quality of the linear fit deteriorates (r^2 values reduce from 0.75 to 0.65 for fringe data and from 0.84 to 0.70 for the forest data), suggesting that the drag was dominated by the near-bottom friction induced by pneumatophores rather than by the larger but sparser tree trunks.

Winds and waves could modify the balance in Eq. (1) by inducing wind or wave set up, particularly on the mudflat and near the fringe. Indeed, departures from Eq. (1) were clear during the high wind and wave conditions of the 'Flats to Forest' experiment in 2015 (Fig. 5b). During this experiment, wind speeds were between 3.5 and 6 ms^{-1} and significant wave heights on the flats were up to 0.3 m. Substantial scatter is apparent in both mudflat and fringe data (blue, orange points) and drag coefficients obtained from the fits were $C_D = 0.18$ in

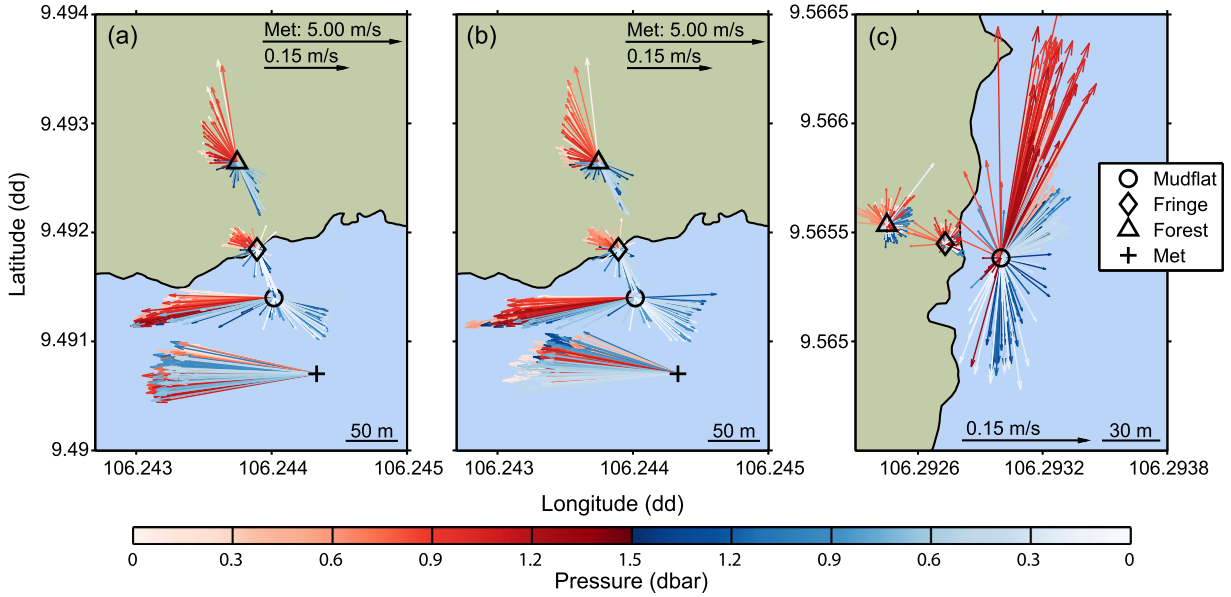

Fig. 4. Arrows indicating water and wind speeds during the 'Flats to Forest' (panels a and b, 2 days each) and 'NE side' experiments in 2015 (panel c). Note the different scales between wind and water speeds. The colour of arrows indicates different stages of the tide (red/orange flood tide and light/dark blue are ebb tides).

Table 2
Summary of pneumatophore measurements. In each case the mean statistic is followed by the maximum values in brackets.

Location	Number of quadrats	Density, n (stems/m^2)	Height (m)	Basal Diameter (mm)
SW fringe	4	115, (159)	0.18, (0.82)	12, (37)
SW forest	3	69, (85)	0.07, (0.62)	9, (36)
NE fringe	1	88, (88)	0.21, (0.61)	11, (49)
NE forest	1	84 (84)	0.14, (0.6)	18, (55)

the fringe and $C_D = 0.019$ in the forest (with $r^2 = 0.49$ and 0.81, respectively). For both years, p-values associated with the gradients of all regression lines were $\ll 0.05$, and differences in C_D between the two regions were statistically significant.

4.2. Along-shore drag balance

A second expression for drag coefficients can be obtained from the measured flow rotations. Neglecting waves, inertial terms and assuming steady state as before, an along-shore balance between pressure gradient, wind, and friction, gives

$$C_{D_+}|\mathbf{u}_+|v_+ = -gh\frac{\partial \eta_+}{\partial y}, \quad \text{(inside forest)}, \tag{2}$$

$$C_{D_-}|\mathbf{u}_-|v_- = -gh\frac{\partial \eta_-}{\partial y} + \tau, \quad \text{(outside forest)}, \tag{3}$$

where subscripts + and - denote values immediately onshore and offshore of the fringe, respectively, and v = along-shore water velocity, the along-shore wind stress inside the forest is neglected, and the along-shore wind stress τ outside the forest is estimated as

$$\tau = \frac{\rho_a}{\rho_w} C_a |\mathbf{u_a}| v_a, \tag{4}$$

in which ρ_a and ρ_w are the density of air and water, respectively. Velocities with subscript a denote wind velocities and C_a is the air-side drag coefficient. Equating the along-shore pressure gradients on either side of the fringe (i.e. $\partial\eta_+/\partial y = \partial\eta_-/\partial y$, to ensure continuity of pressure across the fringe) yields

$$(1 + r_-^2)^{1/2} r_- = \left(\frac{C_{D_+}}{C_{D_-}}\right)(1 + r_+^2)^{1/2} r_+ + \left(\frac{\tau}{C_{D_-} u_+^2}\right), \tag{5}$$

in which we have used $u_+ = u_-$ (by mass conservation) and defined $r = v/u = \tan(\theta)$, where θ is the angle relative to fringe-perpendicular. The second term on the right-hand side of (5) is a measure of the relative importance of wind stress to drag, and can be written as parameter R using (4),

$$R = \frac{\rho_a C_a |\mathbf{u_a}| v_a}{\rho_w C_{D_-} u_+^2}. \tag{6}$$

Taking $\rho_a/\rho_w \approx 1.3 \times 10^{-3}$ and $C_a/C_{D_-} \approx 1$ (Donelan, 1990), (6) can be reduced to

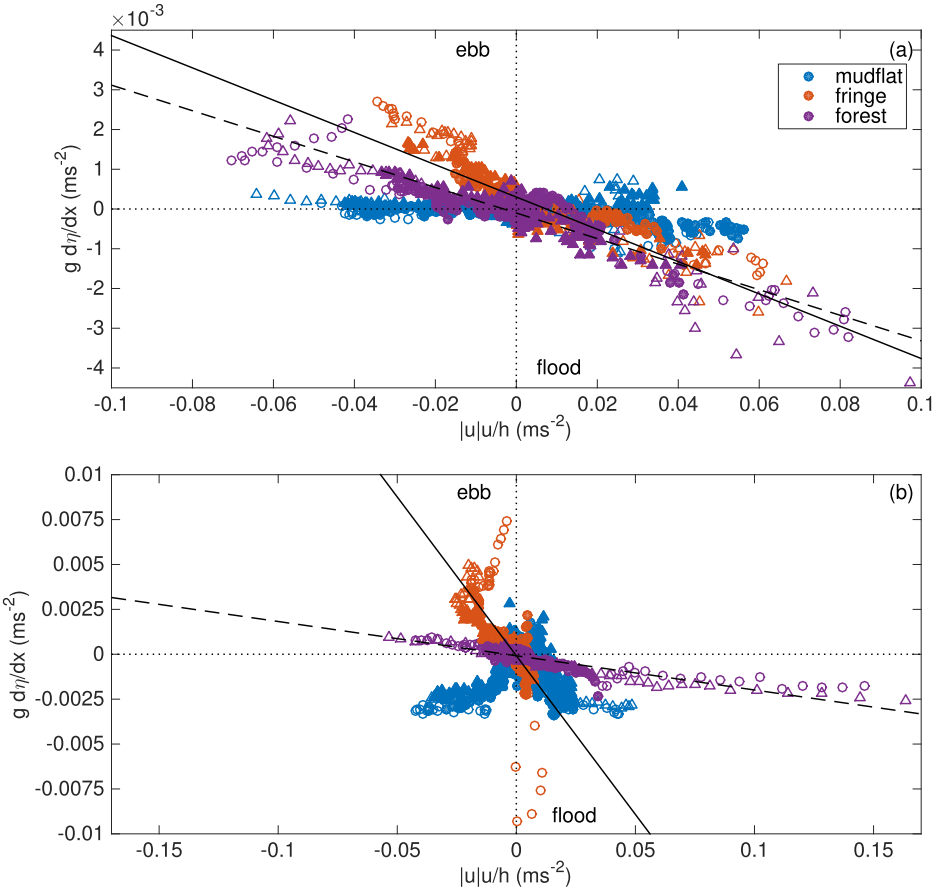

Fig. 5. Data from the across-shore pressure balance (1) for (a) 'Flats to Forest' experiment in September 2014, and (b) 'Flats to Forest' experiment in March 2015. See Fig. 1c,d for instrument locations. Colours indicate the force balance over different regions of the system (blue - mudflat, orange - fringe and purple - forest) and the symbols (triangles and circles) indicate two different tides. Unfilled symbols indicate low water depths (0.25–0.5 m) and filled symbols show water depths >0.5 m. The solid and dashed lines show linear fits to fringe and forest data, respectively. The gradient of the fit gives estimates for the bulk drag coefficients: $C_D = 0.041$ (fringe) and $C_D = 0.032$ (forest) in 2014 and $C_D = 0.18$ (fringe) and $C_D = 0.019$ (forest) in 2015. (Pressure gradients on the mudflat were too small to be accurately resolved).

$$R = 1.3 \times 10^{-3} \times \frac{|\mathbf{u_a}|v_a}{u_+^2}. \quad (7)$$

In cases with no wind, (5) reduces to an expression for ratios of drag coefficients inside and outside of the forest

$$\frac{C_{D+}}{C_{D-}} = \frac{(1 + r_-^2)^{1/2} r_-}{(1 + r_+^2)^{1/2} r_+}, \quad (8)$$

which is a nonlinear analog of standard expressions for flow rotation at a boundary between porous materials of different hydraulic conductivity (e.g. Eq. 5.54 of Bear, 1979). We will use (8) to determine whether observed flow rotations were consistent with tidal currents and the drag coefficients estimated in Section 4.1, and we will use (7) to examine whether discrepancies can be explained by wind forcing.

The expressions above were evaluated using data from the 'Flats to Forest' experiment in 2015 (see Figs. 1d and 4). During this experiment, winds were moderate (3.2 to 7.7 ms^{-1} with an average speed of 5.3 ms^{-1}) and predominantly along-fringe. Significant wave heights of up to $H_s = 0.32$ m were observed on the flats. When evaluating the ratio r, low across-shore velocities introduce substantial scatter, so, in the analysis that follows, cases with very low velocities ($u_+ < 0.04$ ms^{-1}) have been discarded. Results from the fringe (triangles) and forest (circles) are shown in Fig. 6 and have been separated into cases with smaller values of the parameter R ($R < 17$, unfilled symbols) and larger R ($R > 17$, filled symbols). This 'critical' value for R has been arbitrarily selected to show overall trends; however, in general, greater R corresponds to shallow depths and/or greater wind speeds. In these shallow cases, the neglect of depth variability in (7) and (8) may lead to significant model errors (in these cases, the small difference in seabed elevation between flats and fringe/forest locations was appreciable compared with the total depth). The gradient and intercept of the linear fits give bulk estimates for C_{D+}/C_{D-} and R. Fits for smaller R (solid lines), give drag-coefficient ratios of 16 (fringe) and 19 (forest), ($r^2 = 0.38$ and 0.5, with p-values <0.05) and bulk R values in the forest of 19. At the fringe, the bulk R value is not statistically different from 0 (p-value >0.05). Differences between fit parameters across the fringe and forest were not statistically significant (with the exception of the bulk R values). Moreover, including all values for R, does not significantly change fit parameters, yielding only slightly larger drag coefficient ratios of 18 (fringe) and 26 (forest) and bulk $R = 17$ in the forest. These values are in reasonable order-of-magnitude agreement with those from Section 4, although, in contrast to earlier estimates, these values imply larger drag coefficients in the forest interior. These differences could result from the neglect of advective terms (especially $u\partial v/\partial x$) in the force balance. Additionally, the effects of wave breaking were not considered, despite visual observations of wave breaking in the fringe region on some days in 2015 (with relatively rare breaking in the interior).

The effect of waves is examined by considering results from the 'Fine Scale Study' (FSS) of 2015. Over the three days of this experiment, significant wave heights varied from moderate (0.3 m) to the largest observed during the field campaign (0.7 m). The drag balance from Eq. (5) (equivalent to Fig. 6) is shown in Fig. 7 and the changes with wave forcing are clearly apparent. As wave heights increase, both the intercept and gradient of the fit lines increase. The drag-coefficient ratios are estimated as $C_{D+}/C_{D-} = 5.5$, 5.8 and 14.5 and bulk-R = 6.1, 7.6 and 0.88 for experiments with increasing wave heights (day 2, day 1 and day 3 of the FSS experiment). Fits were of high quality with $r^2 = 0.85$, 0.76 and 0.88 with all p-values $\ll 0.05$. The difference in drag coefficients was not significant between days 1 and 2, when waves heights were very similar, however, the increased ratio of drag coefficient from day 3 is significant (corresponding to the much steeper purple line). Differences between bulk-R values were only significant when comparing day 1 to the others days. We note that in general the values on the ordinate are lower for the FSS experiment (Fig. 7) than F2F (Fig. 6), which just represents the different flow directions on the mudflat during this experiment. We conclude that forcing of currents by breaking waves may account for significant departures from (8) on days with relatively energetic waves.

5. Numerical model

5.1. Model set up

To explore the dynamics of flow rotation in the mangrove forest, we set up a schematic numerical model using Delft3D-FLOW (Lesser et al., 2004). Delft3D-FLOW is a process-based hydrodynamic solver for the unsteady non-linear shallow-water equations that has been used in a number of studies of vegetation effects on flow characteristics (e.g. Horstman et al., 2015; Ashall et al., 2016). In the present study, we use Delft3D-FLOW in pure hydrodynamic, 2D depth-averaged mode. For a full 3D model of the Mekong River system, see Thanh et al., (2017).

The setup of our model is as follows. The domain is 12 and 10 km long in the along-shore and across-shore directions, with 52 and 265 grid cells, respectively. The grid cell size varies between 250 m offshore and in the interior of the forest to 5 m at the forest fringe. The bed slope was set to 1 in 1000, consistent with field observations (Bryan

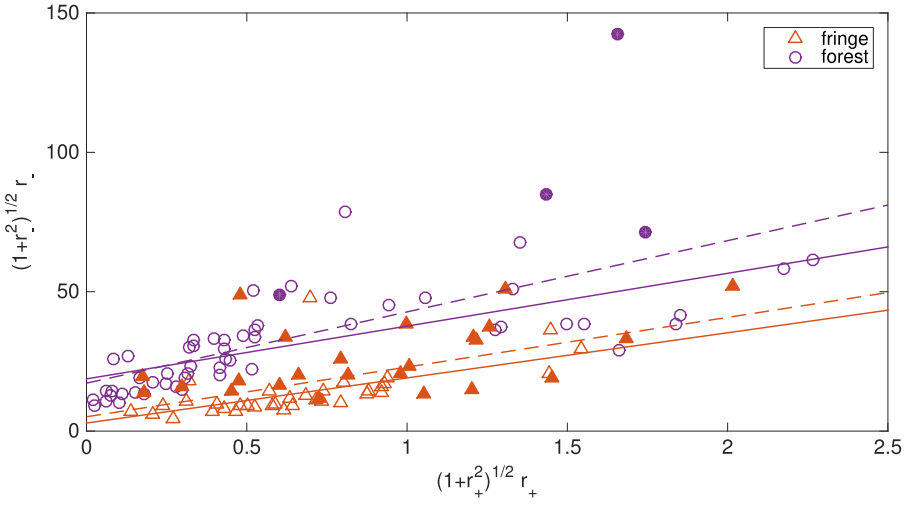

Fig. 6. Rotation values from the forest compared to those from the mudflat for 'Flats to Forest' experiment in 2015 over 4 flood tides. The graph shows $(1 + r_+^2)^{1/2} r_+$ plotted against $(1 + r_-^2)^{1/2} r_-$, with each point being an average over 5 min (see Eq. (5)). Points have been separated into $R < 17$ (unfilled symbols) and $R > 17$ (filled symbols). Lines show fits to low R values (solid lines) and all data (dashed lines). The slope and gradient of the fit lines give bulk estimates of C_{D+}/C_{D-} and bulk parameter R, respectively. See text for details.

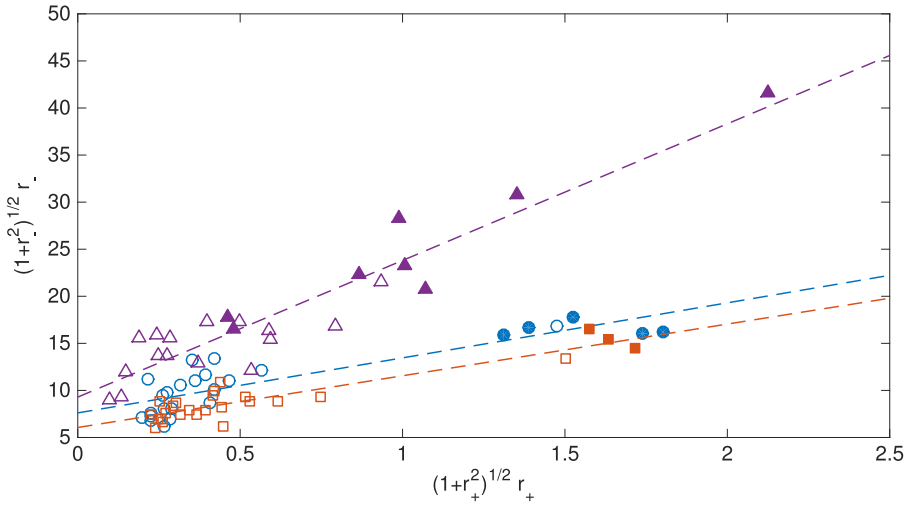

Fig. 7. Rotation values from the forest compared to those from the mudflat for 'Fine Scale Study' experiment in 2015 over 6 flood tides. The graph shows $(1 + r_+^2)^{1/2} r_+$ plotted against $(1 + r_-^2)^{1/2} r_-$, with each point being an average over 5 min (see Eq. (5)). Points have been separated into $R < 17$ (unfilled symbols) and $R > 17$ (filled symbols). Lines show fits to all data (dashed lines). Data have been split into three days of two tides each. Mean significant wave heights over each day were 0.30 m (orange squares), 0.33 m (blue circles) and 0.5 m (purple triangles). The slope of the linear fits gives estimates of C_{D+}/C_{D-} as 5.5 (orange squares), 5.8 (blue circles) and 14.5 (purple triangles).

et al., 2017). A spatially varying roughness is used, and specified as a Chézy value, in order to simulate the differing flow behaviours on the non-vegetated intertidal flat, and the forest featuring pneumatophores and trees. While Delft3D-FLOW can simulate vertically distributed vegetation drag, accounting for stem height and density (Klopstra et al., Baptist et al., 2007), we simply used variable Chézy coefficients to facilitate comparison with the variable drag coefficients noted in Section 4. The specified roughness transitioned linearly from mudflat to forest values over a 30-m simulated transition zone. The viscosity and diffusivity, respectively representing vertical and lateral mixing, were set to spatially uniform values of 1 m^2s^{-1} and 0.1 m^2s^{-1}, respectively. Coriolis forcing was neglected. The offshore water-level boundary forcing consisted of a semi-diurnal progressive tide of 1 m or 2 m range, resulting in maximum water depths at the fringe of 1.8 m and 2.3 m. The lateral boundaries were imposed as water-level gradient boundaries (Roelvink and Walstra, 2004). A predominantly along-shore directed wind with a small onshore component (20% of along-shore component) was imposed only on the non-vegetated tidal flat, to mimic the observed absence of appreciable wind forcing inside the forest. Air pressure was assumed to be spatially uniform with a value of 1013 hPa. The time step was 3 s. Parameters used in the numerical simulations are shown in Table 3. Chézy values of 5, 15 and 65 correspond to bottom friction coefficients of 0.39, 0.044 and 0.0023, respectively (Deltares, 2017).

5.2. Results

The numerical simulations reproduced the flow rotation, with instantaneous across-shore velocities remaining similar inside and outside of the forest, but the along-shore velocities were greatly reduced (Fig. 8a,d). Depth-averaged flow speeds for a 2-m tidal range were around 0.2 to 0.3 ms^{-1} on the mudflat close to the fringe, roughly consistent with field observations (which were measured closer to the bed). Simulated bed stresses were larger during the ebb than flood tide, with maximum values occurring at the fringe and in the forest during the flood and ebb, respectively (Figs. 8b,c,e,f).

Snapshots of the across- and along-shore momentum balances for a fringe water depth of 1.2 m are shown in Figs. 9a and 9b, respectively, for the case with no wind forcing and Figs. 10a and 10b, respectively, for a case with strong wind forcing (10 ms^{-1} in the along-shore direction). In the across-shore direction on the mudflat and in the forest, the bed shear stress is balanced by the pressure gradient with close to zero contributions from the other terms. The dominant balances in the along-shore direction change between the flats and the forest. Inside the forest the dominant balance remains between the bed shear stress and pressure gradient. Farther out on the mudflat, the bed shear stress is predominantly balanced by pressure gradient in cases with no wind, but is balanced by the wind forcing for cases with strong winds. There are some additional contributions from lateral momentum exchange in the region immediately adjacent to the forest $x \approx -250$ m to x=0. This contribution becomes more important closer to the forest (as the contribution from wind correspondingly decreases). However in both cases, the along-shore momentum balance shows that lateral momentum exchange is non-negligible in a ~80-m-wide region around the fringe, corresponding to the start of the transition zone over which the change in roughness coefficients is applied. In this region the acceleration due to the shear stress (~0.00041 and 0.0012 m/s^2 for Figs. 9b and 10b) is mostly balanced by the acceleration due to lateral momentum exchange (~0.0011 and 0.0004 m/s^2 in Figs. 9b and 10b, respectively). Hence, the neglect of advective terms in (5) is likely to cause errors near the fringe. However, farther into the forest, the balance appears to hold.

As noted above, winds do not contribute substantially in the across-shore momentum balance, however in the along-shore direction the contribution of strong winds (>10 ms^{-1}) significantly enhances the bed shear stresses on the tidal flat (0.1 Nm^{-2}, compared to values of 0.03 Nm^{-2} for wind speeds of 5 ms^{-1}). Weaker winds have little effect in the force balance. Around the fringe zone, where the wind influence decreases because of the presence of trees, bed shear stress is again balanced by lateral momentum exchange.

The runs exploring the effects of a larger vegetation density (represented by a smaller Chézy value), demonstrated similar balances, except that the width of the region near the forest with high values of lateral momentum exchange was narrower (e.g. for C_+/C_- of 0.077 the width was 25 m compared with the width 80 m in Fig. 8). in other words, the change in flow direction occurred more abruptly over a narrower region for this

Table 3
Summary of numerical parameters.

Run numbers	Chézy valuesflats, forest ($m^{1/2}s^{-1}$)	Tidal range (m)	Along-shore windspeed (ms^{-1})
1–4	65, 5	1	0, 2, 5, and 10
5–8	65, 5	2	0, 2, 5, and 10
9–12	65, 15	1	0, 2, 5, and 10
13–16	65, 15	2	0, 2, 5, and 10

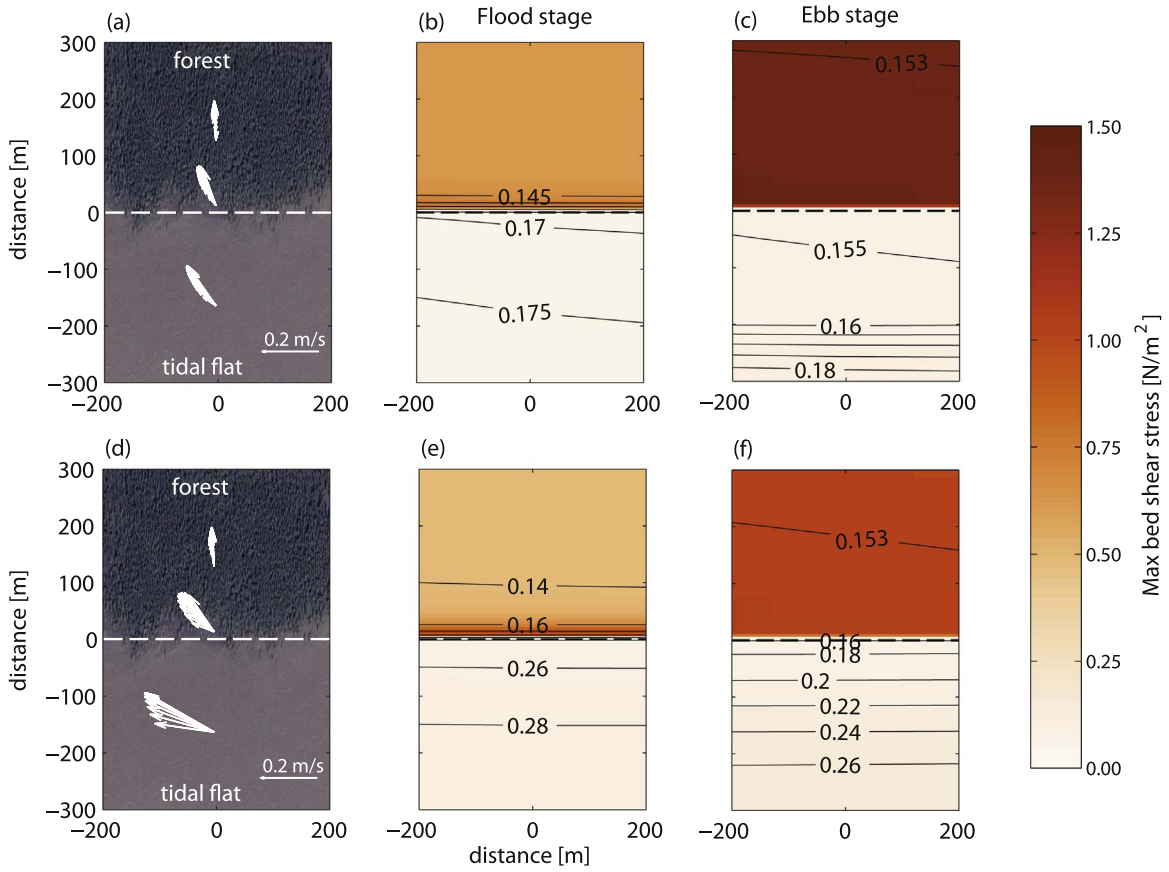

Fig. 8. (a) Example of flow rotation during a flooding tide, from numerical simulations with an offshore tidal range of 2 m, no wind forcing and a ratio of Chézy roughness values of C_+/C_- of 0.23 (corresponding to $C_{D+}/C_{D-} \approx 20$), (run 13, Table 3). The vectors represent 10-min averaged model output plotted once every 50 min. Depths ranged between 0.35 and 1.6 m inside the forest. Background image: Google Earth. Maximum bed shear stress (colors) and maximum velocities (black contours) during flood (b) and ebb (c) phases of the tide. (d-f) are the same as (a-c) except show the case with an along-shore wind speed of 10 ms^{-1} (run 16, Table 3). Contour intervals are 0.05 ms^{-1} in (b,c) and 0.02 in (e,f) unless explicitly indicated otherwise.

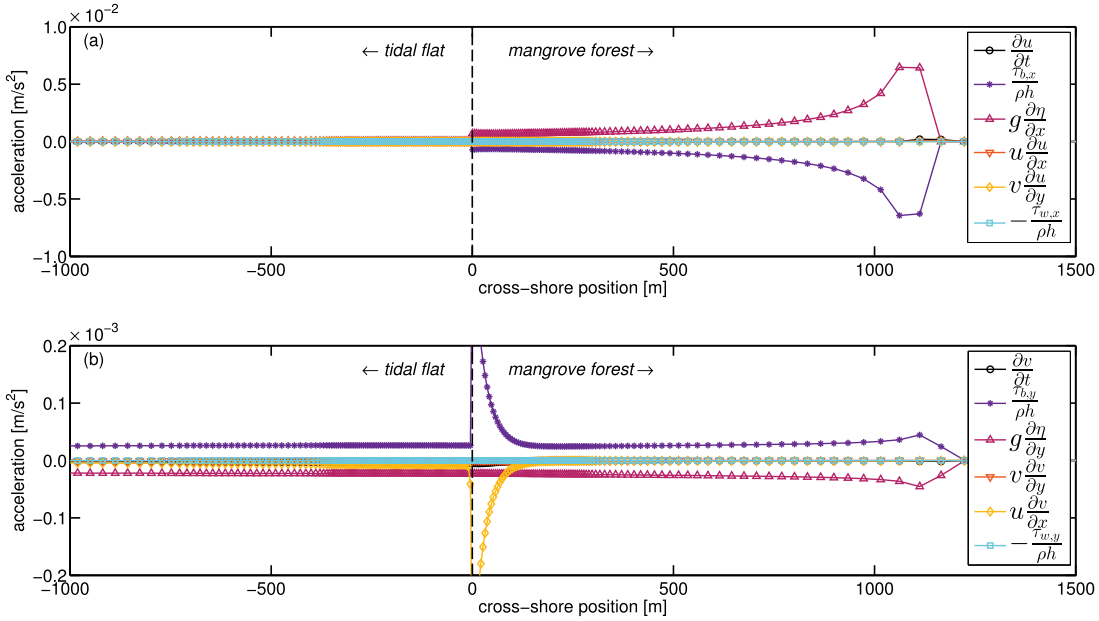

Fig. 9. Momentum balance in the (a) across-shore direction for a simulation with an offshore tidal range of 2 m, no wind forcing, and a ratio of Chézy roughness values of C_+/C_- of 0.23 (corresponding to $C_{D+}/C_{D-} \approx 20$) (run 13, Table 3). The depth in the forest fringe is 1.2 m. Accelerations due to inertia ($\partial u/\partial t$, circles), acceleration due to bed shear stress ($\tau_{b,x}/\rho h$, stars), acceleration due to the across-shore pressure gradient ($g\partial\eta/\partial x$, triangles), acceleration due to streamwise momentum exchange ($u\partial u/\partial x$, inverted triangles), acceleration due to lateral momentum exchange ($v\partial u/\partial y$, diamonds), and acceleration due to across-shore wind forcing ($-\tau_{w,x}/\rho h$, squares). The dashed line shows the position of the vegetation fringe and the edge of the transition zone between the 'forest' and 'mudflat' drag coefficients. (b) shows the equivalent terms in the along-shore direction. In (b) the peaks in acceleration at the fringe due to bed shear stress and lateral momentum exchange reach 0.00041 and −0.0004, respectively.

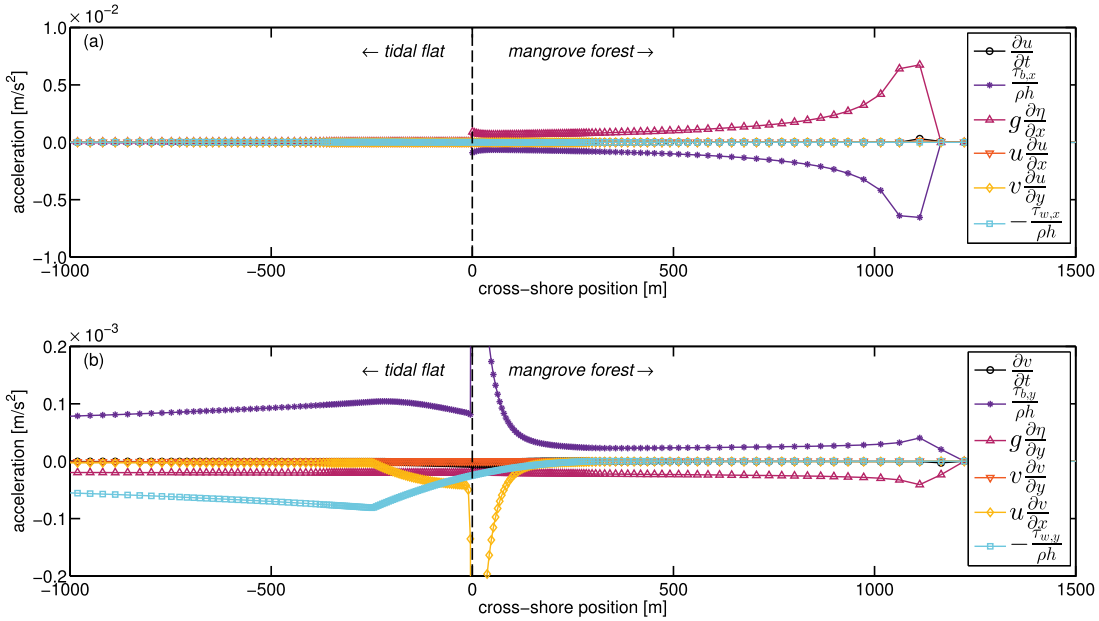

Fig. 10. Momentum balance in the (a) across-shore direction for a simulation with an offshore tidal range of 2 m, an along-(across-) shore wind velocity of 10 (2)ms^{-1}, and a ratio of Chézy roughness values of C_+/C_- of 0.23 (corresponding to $C_{D+}/C_{D-} \approx 20$) (run 16, Table 3). The depth in the forest fringe is 1.2 m. Accelerations due to inertia ($\partial u/\partial t$, circles), acceleration due to bed shear stress ($\tau_{b,x}/\rho h$, stars), acceleration due to the across-shore pressure gradient ($g\partial\eta/\partial x$, triangles), acceleration due to streamwise momentum exchange ($u\partial u/\partial x$, inverted triangles), acceleration due to lateral momentum exchange ($v\partial u/\partial y$, diamonds), and acceleration due to across-shore wind forcing ($-\tau_{w,x}/\rho h$, squares). The dashed line shows the position of the vegetation fringe and the edge of the transition zone between the 'forest' and 'mudflat' drag coefficients. (b) shows the equivalent terms in the along-shore direction. In (b) the peaks in acceleration at the fringe due to bed shear stress and lateral momentum exchange reach 0.0012 and −0.0011, respectively.

case of higher simulated density. The absolute values of the dominant two terms were also larger, with acceleration due to bed shear stress and that due to lateral momentum exchange reaching 0.0027 and 0.0024, respectively. Moreover, the pressure gradient and advection terms were smaller when compared to the lower friction case.

5.3. Discussion of dynamics and comparison with previous work

We have presented field observations of flow rotation as the tide enters a tropical forest in the Mekong Delta. Such flow rotation has previously been observed in other, very different, mangrove environments. Horstman et al., (2013, 2015) observed and modelled flow rotation in a low-energy mangrove forest in Thailand incised by creeks and similar flow patterns have also been observed in subtropical riverine mangrove forests (Kobashi and Mazda, 2005). Chen et al. (2016) reported flow rotation in an upper-estuary tidal flat and mangrove system in southeast China. In our study, a rapid and pronounced reduction of flow speeds occurred within very short distances after flow entered the vegetated region; along-shore flow speeds reduced by 75% within tens of meters of the boundary, similar to Chen et al. (2016) who observed 50% of flow speeds within 10 m of the mangrove edge.

A simple balance between drag and pressure forcing appears to hold in the forest interior. Linear fits to this balance give drag coefficients of 0.03–0.04 for flow over pneumatophore canopies. These values are ~20 times larger than values typically associated with similar but unvegetated environments. (For shallow water depths with emergent or barely submerged pneumatophores, our results here are not conclusive but are weakly suggestive of higher drag coefficients). Logarithmic boundary-layer models predict a drag coefficient of $[0.4/\log(z/z_0)]^2$, where z = velocity measurement elevation and z_0 = bottom roughness length. Therefore, representing the observed drag with such a model would require a bottom roughness of ~4 cm. The drag coefficients obtained in the present study are an order of magnitude smaller than those calculated by Chen et al. (2016). These differences likely result from major differences in tree morphology. Given the large trunk-to-trunk spacing of the large *Sonneratia* trees considered here, the well-developed aerial root systems may have contributed significantly to total drag. This suggestion is supported by the relatively poor performance of the emergent stem model (Section 4). In contrast, the study by Chen et al. (2016) was in a mangrove forest dominated by young *Kandelia obovata* and *Aegiceras corniculatum*, that did not have a well-developed root system. The mean tree height was 1.6 m compared with the O(10 m) trees we observed, and water depths were sufficient that the lower part of the tree canopy (including leaves and branches) was submerged. Hence, in their system drag was provided by the whole trees themselves.

Vegetation density was an important control on drag, with largest values of drag observed at the forest fringe (Fig. 5), the location at which pneumatophores were largest and densest (Norris et al., 2017). Moreover, the dynamics at the fringe were considerably more complex than in the forest interior. The obliquely incident flow (driven in part by strong along-shore winds) likely advects along-shore momentum into the fringe, modifying the momentum balance. The dynamics of the fringe were further modified by the presence of both breaking and non-breaking waves. Although neglected in the drag balance, experiments with larger waves yielded larger estimates of drag coefficients. Within pneumatophores, waves can increase turbulence and drag, and can generate additional flows ('wave streaming') with the potential to transport sediment (Luhar et al., 2013). Wave breaking in the fringe region may provide additional forcing of along-shore currents (by generating radiation stress gradients), as is often observed on beaches (Longuet-Higgins, 1970a, 1970b).

Coastal vegetation encompasses a wide variety of geometric characteristics (Mullarney and Henderson, 2017). The pneumatophores in the present study were, in general, wider and taller, but less dense than salt marsh vegetation or seagrass. Nonetheless, aspects of the dynamics here are comparable to those observed in other mangrove and salt marsh systems. In particular, Temmerman et al. (2005) and Ashall et al. (2016) report field observations and numerical modelling results of flows in meso- and macro-tidal salt-marsh systems with flooding and draining occurring in a direction perpendicular to the vegetation line.

6. Conclusion

Mangrove forests have been shown to armour coastlines against destructive hydrodynamic forces while simultaneously providing ecological benefits. Over recent decades, these systems have undergone rapid but highly variable changes, with some systems prograding while others retreat (Giri et al., 2011; Swales et al., 2015). Understanding these changes will require examination of the interactions between vegetation, currents, and the sediment supply, as the combined effect may control the evolution of the coastline (Bryan et al., 2017). Drag coefficients have previously been shown to be variable within mangrove forests, owing to the variability in tree and root geometries and the variability of the environmental forcing. Field observations from a mangrove forest on Cù Lao Dung Island in the Mekong Delta, composed predominantly of *Sonneratia*, yielded spatially variable estimates for bottom-drag coefficients, which are ~20 times larger than for non-vegetated systems. The drag coefficients were largest in the mangrove fringe, where the largest and densest pneumatophore canopies were observed. As water flows into the forest, the increase in drag associated with the pneumatophores causes a local change (rotation) in flow direction relative to tidal velocities on the mudflat, with flows becoming close to fringe-perpendicular. Mangroves further reduce flow speeds by sheltering the water surface from wind forcing. Drag was enhanced when water depths were low. The dynamics of the system, particularly within the fringe region were also substantially modulated by the wind and wave energy. These observations shed light on the dominant forcing terms, and quantify the frictional effects, that control the transition from energetic offshore flows to relatively low-energy flows within forests. This transition is fundamental to the ability of mangrove forests to provide sheltered environments of rapid sediment accumulation.

Accurate drag parameterisations are essential to our ability to reliably model the interplay between vegetation and deposition/erosion, and hence, our ability to predict how mangrove systems may evolve under future changes in hydrodynamic forcing and upstream sediment supply. These predictions may ultimately be required to construct and inform mangrove preservation and restoration projects.

Acknowledgments

We thank the Office of Naval Research Global and the Office of Naval Research (USA) for funding (grant numbers N62909-14-1-N028 to JM and KB, N00014-14-10112 to SH and N00014-15-1-2824 to JR), Dean Sandwell for invaluable and heroic assistance with fieldwork and logistics, the sediment dynamics lab from the University of Washington (and in particular Aaron Fricke, Dan Culling, Andrea Ogston and Chuck Nittrouer), Dr H.P. Vo-Luong, Xuan Tien Nguyen Vinh, and Hoang Phong Nguyen from the University of Science (Ho Chi Minh City), and Rich Nguyen from ONR for their immense help in planning, organising and implementing the challenging logistics of the experiments and for assistance in the field, and to Aaron Fricke for providing additional pressure data for the 2014 experiment. Thanks also to Sergio Fagherazzi and William Nardin from Boston University for assistance in the field. We thank three anonymous reviewers and guest editor Chuck Nittrouer for comments which improved the manuscript.

References

Alongi, D.M., 2002. Present state and future of the world's mangrove forests. Environ. Conserv. 29, 331-349. http://dx.doi.org/10.1017/S0376892902000231.

Alongi, D.M., 2008. Mangrove forests: resilience, protection from tsunamis, and responses to global climate change. Estuar. Coast. Shelf Sci. 76, 1–13. http://dx.doi.org/10.1016/j.ecss.2007.08.024.

Anthony, E.J., Brunier, G., Besset, M., Goichot, M., Dussouillez, P., Nguyen, V.L., 2015. Linking rapid erosion of the Mekong River delta to human activities. Sci. Rep.-UK, 5. http://dx.doi.org/10.1038/srep14745.

Ashall, L.M., Mulligan, R.P., van Proosdij, D., Poirier, E., 2016. Application and validation of a three-dimensional hydrodynamic model of a macrotidal salt marsh. Coast. Eng. 114, 35–46. http://dx.doi.org/10.1016/j.coastaleng.2016.04.005.

Bao, T.Q., 2011. Effect of mangrove forest structures on wave attenuation in coastal Vietnam. Oceanologia 53, 807–818. http://dx.doi.org/10.5697/oc.53-3.807.

Baptist, M.J., Babovic, V., Uthurburu, J.R., Keijzer, M., Uittenbogaard, R.E., Mynett, A., Verwey, A., 2007. On inducing equations for vegetation resistance. J. Hydraul. Res. 45, 435–450.

Barbier, E.B., Koch, E.W., Silliman, B.R., Hacker, S.D., Wolanski, E., Primavera, J., Granek, E.F., Polasky, S., Aswani, S., Cramer, L.A., Stoms, D.M., Kennedy, C.J., Bael, D., Kappel, C.V., Perillo, G.M.E., Reed, D.J., 2008. Coastal ecosystem-based management with nonlinear ecological functions and values. Science 319, 321–323. http://dx.doi.org/10.1126/science.1150349.

Bear, J., 1979. Hydraulics of Groundwater. Dover, New York.

Bryan, K.R., Nardin, W., Mullarney, J.C., Fagherazzi, S., 2017. The role of cross-shore tidal dynamics in controlling intertidal sediment exchange in mangroves in Cù Lao Dung, Vietnam. Cont. Shelf Res., this volume, in press.http://dx.doi.org/10.1016/j.csr.2017.06.014.

Bullock, E.L., Fagherazzi, S., Nardin, W., Vo-Luong, H.P., Nguyen, P., Woodcock, C.E., 2017. Temporal patterns in species zonation in a mangrove forest in the Mekong Delta, Vietnam, using a time series of LANDSAT imagery. Cont. Shelf Res., this volume, submitted for publication.

Chen, Y., Li, Y., Cai, T., Thompson, C., Li, Y., 2016. A comparison of biohydrodynamic interaction within mangrove and saltmarsh boundaries. Earth Surf. Proceedings Land. 41, 1967–1979. http://dx.doi.org/10.1002/esp.3964.

Chmura, G.L., Anisfeld, S.C., Cahoon, D.R., Lynch, J.C., 2003. Global carbon sequestration in tidal, saline wetland soils. Glob. Biogeochem. Cy., 17. http://dx.doi.org/10.1029/2002GB001917.

Costanza, R., d'Arge, R., de Groot, R., Farber, S., Grasso, M., Hannon, B., Limburg, K., Naeem, S., O'Neill, R., Paruelo, J., Raskin, R., Sutton, P., van den Belt, M., 1997. The value of the world's ecosystem services and natural capital. Nature 387, 253–260. http://dx.doi.org/10.1038/387253a0.

Danielsen, F., Sorensen, M.K., Olwig, M.F., Selvam, V., Parish, F., Burgess, N.D., Hiraishi, T., Karunagaran, V.M., Rasmussen, M.S., Hansen, L.B., Quarto, A., Suryadiputra, N., 2005. The Asian tsunami: A protective role for coastal vegetation. Science 310, 643. http://dx.doi.org/10.1126/science.1118387.

Deltares, 2017. Delft3D-FLOW User Manual, version 3.15.49946. Deltares.

Donato, D.C., Kauffman, J.B., Murdiyarso, D., Kurnianto, S., Stidham, M., Kanninen, M., 2011. Mangroves among the most carbon-rich forests in the tropics. Nat. Geosci. 4, 293–297. http://dx.doi.org/10.1038/NGEO1123.

Donelan, M., 1990. Air–sea interaction, In: Mehaute, B.L., Hanes, D.M. (Eds.), The Sea, Vol. 9: Ocean Engineering Science. Wiley, pp. 239–292.

Fricke, A.T., Nittrouer, C.A., Ogston, A.S., Vo-Luong, H.P., 2017. Asymmetric progradation of a coastal mangrove forest controlled by combined fluvial and marine influence, Cù Lao Dung, Vietnam. Cont. Shelf Res., this volume, submitted for publication.

Furukawa, K., Wolanski, E., Mueller, H., 1997. Currents and sediment transport in mangrove forests. Estuar. Coast. Shelf Sci. 44, 301–310. http://dx.doi.org/10.1006/ecss.1996.0120.

Giri, C., Ochieng, E., Tieszen, L.L., Zhu, Z., Singh, A., Loveland, T., Masek, J., Duke, N., 2011. Status and distribution of mangrove forests of the world using earth observation satellite data. Glob. Ecol. Biogeogr. 20, 154–159. http://dx.doi.org/10.1111/j.1466-8238.2010.00584.x.

Goring, D.G., Nikora, V.I., 2002. Despiking acoustic Doppler velocimeter data. J. Hydraul. Eng. -ASCE 128, 117–126. http://dx.doi.org/10.1061/(ASCE)0733-9429(2002)128:1(117)s.

Henderson, S.M., Norris, B.K., Mullarney, J.C., Bryan, K.R., 2017. Wave-frequency flows within a near-bed vegetation canopy. Cont. Shelf Res., this volume, https://dx.doi.org/10.1016/j.csr.2017.06.003.

Horstman, E.M., Dohmen-Janssen, C.M., Bouma, T.J., Hulscher, S.J.M.H., 2015. Tidal-scale flow routing and sedimentation in mangrove forests: combining field data and numerical modelling. Geomorphology 228, 244–262. http://dx.doi.org/10.1016/j.geomorph.2014.08.011.

Horstman, E.M., Dohmen-Janssen, C.M., Hulscher, S.J.M.H., 2013. Flow routing in mangrove forests: a field study in Trang province, Thailand. Cont. Shelf Res. 71, 52–67. http://dx.doi.org/10.1016/j.csr.2013.10.002.

Horstman, E.M., Dohmen-Janssen, C.M., Narra, P.M.F., van den Berg, N.J.F., Siemerink, M., Hulscher, S.J.M.H., 2014. Wave attenuation in mangroves: a quantitative approach to field observations. Coast. Eng. 94, 47–62. http://dx.doi.org/10.1016/j.coastaleng.2014.08.005.

Kathiresan, K., Bingham, B.L., 2001. Biology of mangroves and mangrove ecosystems. Adv. Mar. Biol. 40, 81–251.

Kirwan, M.L., Guntenspergen, G.R., D'Alpaos, A., Morris, J.T., Mudd, S.M., Temmerman, S., 2010. Limits on the adaptability of coastal marshes to rising sea level. Geophys. Res. Lett., 37. http://dx.doi.org/10.1029/2010GL045489.

Kirwan, M.L., Temmerman, S., Skeehan, E.E., Guntenspergen, G.R., Fagherazzi, S., 2016. Overestimation of marsh vulnerability to sea level rise. Nat. Clim. Change 6, 253–260. http://dx.doi.org/10.1038/NCLIMATE2909.

Klopstra, D., Barneveld, H.J., Van Noortwijk, J.M., Van Velzen, E.H., 1997. Analytical model for hydraulic roughness of submerged vegetation, In: Proceedings of The 27th IAHR Congress: Theme A, Managing Water: Coping with Scarcity and Abundance, American Society of Civil Engineers (ASCE), New York. pp. 775–780.

Knutson, T.R., McBride, J.L., Chan, J., Emanuel, K., Holland, G., Landsea, C., Held, I., Kossin, J.P., Srivastava, A.K., Sugi, M., 2010. Tropical cyclones and Climate Change. Nat. Geosci. 3, 157–163. http://dx.doi.org/10.1038/NGEO779.

Kobashi, D., Mazda, Y., 2005. Tidal flow in riverine-type mangroves. Wetl. Ecol. Manag 13, 615–619. http://dx.doi.org/10.1007/s11273-004-3481-4.

Krauss, K.W., Allen, J.A., Cahoon, D.R., 2003. Differential rates of vertical accretion and

elevation change among aerial root types in Micronesian mangrove forests. Estuar. Coast. Shelf Sci. 56, 251–259. http://dx.doi.org/10.1016/S0272-7714(02)00184-1.
Lesser, G.R., Roelvink, J.A., van Kester, J.A.T.M., Stelling, G.S., 2004. Development and validation of a three-dimensional morphological model. Coast. Eng. 51, 883–915. http://dx.doi.org/10.1016/j.coastaleng.2004.07.014.
Liénard, J., Lynn, K., Strigul, N., Norris, B.K., Gatziolis, D., Mullarney, J.C., Bryan, K.R., Henderson, S.M., 2016. Efficient three-dimensional reconstruction of aquatic vegetation geometry: Estimating morphological parameters influencing hydrodynamic drag. Estuar. Coast. Shelf Sci. 178, 77–85. http://dx.doi.org/10.1016/j.ecss.2016.05.011.
Lohrmann, A., Hackett, B., Røed, L.P., 1990. High resolution measurements of turbulence, velocity and stress using a pulse-to-pulse coherent sonar. J. Atmos. Ocean. Tech. 7, 19–37.
Longuet-Higgins, M.S., 1970a. Longshore currents generated by obliquely incident sea waves, 1. J. Geophys. Res. 75, 6778–6789.
Longuet-Higgins, M.S., 1970b. Longshore currents generated by obliquely incident sea waves, 2. J. Geophys. Res. 75, 6790–6801.
Luhar, M., Infantes, E., Orfila, A., Terrados, J., Nepf, H.M., 2013. Field observations of wave-induced streaming through a submerged seagrass (*Posidonia oceanica*) meadow. J. Geophys. Res. -Oceans 118, 1955–1968. http://dx.doi.org/10.1002/jgrc.20162.
Mariotti, G., Fagherazzi, S., 2010. A numerical model for the coupled long-term evolution of salt marshes and tidal flats. J. Geophys. Res. -Earth Surf., 115. http://dx.doi.org/10.1029/2009JF001326.
Massel, S.R., Furukawa, K., Brinkman, R.M., 1999. Surface wave propagation in mangrove forests. Fluid Dyn. Res. 24, 219–249. http://dx.doi.org/10.1016/S0169-5983(98)00024-0.
Mazda, Y., Kobashi, D., Okada, S., 2005. Tidal-scale hydrodynamics within mangrove swamps. Wetl. Ecol. Manag. 13, 647–655.
Mazda, Y., Magi, M., Ikeda, Y., Kurokawa, T., Asano, T., 2006. Wave reduction in a mangrove forest dominated by *Sonneratia* sp. Wetl. Ecol. Manag. 14, 365–378. http://dx.doi.org/10.1007/s11273-005-5388-0.
Mazda, Y., Magi, M., Kogo, M., Hong, P.N., 1997a. Mangroves as a coastal protection from waves in the Tong King Delta, Vietnam. Mangroves Salt Marshes 1, 127–135. http://dx.doi.org/10.1023/A:1009928003700.
Mazda, Y., Wolanski, E., King, B., Sase, A., Ohtsuka, D., Magi, M., 1997b. Drag force due to vegetation in mangrove swamps. Mangroves Salt Marshes 1, 193–199.
Mcleod, E., Chmura, G.L., Bouillon, S., Salm, R., Bjork, M., Duarte, C.M., Lovelock, C.E., Schlesinger, W.H., Silliman, B.R., 2011. A blueprint for blue carbon: toward an improved understanding of the role of vegetated coastal habitats in sequestering CO_2. Front. Ecol. Environ. 9, 552–560. http://dx.doi.org/10.1890/110004.
Mullarney, J.C., Henderson, S.M., 2017. Flows within marine vegetation canopies, In: Panchang, V., Kaihatu, J. (Eds.), Advances in Coastal Hydraulics. World Scientific. In press.
Nardin, W., Locatelli, S., Pasquarella, V., Rulli, M.C., Woodcock, C.E., Fagherazzi, S., 2016. Dynamics of a fringe mangrove forest detected by landsat images in the mekong river delta, vietnam. Earth Surf. Proceedings Land. 41, 2024–2037. http://dx.doi.org/10.1002/esp.3968.
Nepf, H.M., 1999. Drag, turbulence, and diffusion in flow through emergent vegetation. Water Resour. Res. 35, 479–489. http://dx.doi.org/10.1029/1998WR900069.
Nguyen, H.H., McAlpine, C., Pullar, D., Johansen, K., Duke, N.C., 2013. The relationship of spatial-temporal changes in fringe mangrove extent and adjacent land-use: Case study of Kien Giang coast, Vietnam. Ocean Coast. Manag. 76, 12–22. http://dx.doi.org/10.1016/j.ocecoaman.2013.01.003.
Nicholls, R.J., Hoozemans, F.M.J., Marchand, M., 1999. Increasing flood risk and wetland losses due to global sea-level rise: regional and global analyses. Glob. Environ. Chang. 9, S69–S87. http://dx.doi.org/10.1016/S0959-3780(99)00019-9.
Norris, B.K., Mullarney, J.C., Henderson, S.M., Bryan, K.R., 2017. The dependence of turbulence on rigid plant density: A field study in a fringing mangrove forest. Cont. Shelf Res., this volume, in press. https://doi.org/10.1016/j.csr.2017.06.002.
Nowacki, D.J., Ogston, A.S., Nittrouer, C.A., Fricke, A.T., Van, P.D.T., 2015. Sediment dynamics in the lower Mekong River: transition from tidal river to estuary. J. Geophys. Res. -Oceans 120, 6363–6383. http://dx.doi.org/10.1002/2015JC010754.
Perillo, G.M.E., Wolanski, E., Cahoon, D.R., Brinson, M.M., 2009. Coastal Wetlands: An Integrated Ecosystem Approach. Elsevier.
Roelvink, J.A., Walstra, D.J., 2004. Keeping it simple by using complex models. Adv. Hydro-Sci. Eng. 6, 1–11.
Sallenger, A.H., Jr., Doran, K.S., Howd, P.A., 2012. Hotspot of accelerated sea-level rise on the Atlantic coast of North America. Nat. Clim. Change 2, 884–888. http://dx.doi.org/10.1038/NCLIMATE1597.
Struve, J., Falconer, R.A., Wu, Y., 2003. Influence of model mangrove trees on the hydrodynamics in a flume. Estuar. Coast. Shelf Sci. 58, 163–171. http://dx.doi.org/10.1016/S0272-7714(03)00072-6.
Swales, A., Bentley, S.J., Lovelock, C.E., 2015. Mangrove-forest evolution in a sediment-rich estuarine system: opportunists or agents of geomorphic change? Earth Surf. Proc. Land. 40, 1672–1687. http://dx.doi.org/10.1002/esp.3759.
Temmerman, S., Bouma, T.J., Govers, G., Wang, Z.B., De Vries, M.B., Herman, P.M.J., 2005. Impact of vegetation on flow routing and sedimentation patterns: three-dimensional modeling for a tidal marsh. J. Geophys. Res. -Earth Surf., 110. http://dx.doi.org/10.1029/2005JF000301.
Thanh, V., Reyns, J., Wackerman, C., Eidam, E.F., Roelvink, J.A., 2017. Modelling suspended sediment dynamics on the delta shelf of the Mekong River. Cont. Shelf Res., this volume, submitted for publication.
Thu, P.M., Populus, J., 2007. Status and changes of mangrove forest in Mekong Delta: case study in Tra Vinh, Vietnam. Estuar. Coast. Shelf Sci. 71, 98–109. http://dx.doi.org/10.1016/j.ecss.2006.08.007.
van Maanen, B., Coco, G., Bryan, K.R., 2015. On the ecogeomorphological feedbacks that control tidal channel network evolution in a dynamic mangrove setting. In: Proceedings R. Soc. A 471. http://dx.doi.org/10.1098/rspa.2015.0115.
Vo-Luong, H.P., Massel, S., 2008. Energy dissipation in non-uniform mangrove forests of arbitrary depth. J. Mar. Syst. 74, 603–622. http://dx.doi.org/10.1016/j.jmarsys.2008.05.004.
Walsh, J.P., Nittrouer, C.A., 2004. Mangrove-bank sedimentation in a mesotidal environment with large sediment supply. Gulf Papua Mar. Geol. 208, 225–248. http://dx.doi.org/10.1016/j.margeo.2004.04.010.
Wolanski, E., 2007. Protective functions of coastal forests and trees against natural hazards, In: Braatz, S., Fortuna, S., Broadhead, J., Leslie, R. (Eds.), Coastal Protection in the Aftermath of the Indian Ocean Tsunami: what role for forests and trees?. Food and Agriculture Organization of the United Nations, Regional Office for Asia and the Pacific, Bangkok, Thailand, pp. 157–179.
Wolanski, E., Huan, N.N., Dao, L.T., Nhan, N.H., Thuy, N.N., 1996. Fine-sediment Dynamics in the Mekong River Estuary, Vietnam. Estuar. Coast. Shelf Sci. 43, 565–582.
Wolanski, E., Jones, M., Bunt, J.S., 1980. Hydrodynamics of a tidal creek mangrove swamp system. Aust. J. Mar. Fresh. Res. 31, 431–450.
Wright, L.D., 1985. River deltas, in: Davis, R.A. (Ed.), Coastal SedimentaryEnvironments. Springer New York, New York, NY, pp. 1{76. doi:10.1007/978-1-4612-5078-4_1.